

Tailored Synthesis of Conformal Si-Al Coatings on TiO₂ Nanotubes for Hybrid Negative Electrodes of Lithium-Ion Batteries

Abirdu Woreka Nemaga, Claude Guery, Michael Molinari, Jean Michel, Mathieu Morcrette,* and Jeremy Mallet*

An original synthesis route has been developed to optimize silicon's utility in replacing graphite as anode material in Li-ion batteries. This involves blending silicon with aluminum to enhance its conductivity. The silicon-aluminum is codeposited on a nanoporous titanium dioxide nanotube matrix, which serves as an active current collector, thereby eliminating the need for inactive binders and ensuring robust mechanical stability during cycling. The nanostructured negative electrode is fabricated through two electrochemical synthesis steps: first, the

anodization of a titanium foil, followed by the coelectrodeposition of silicon and aluminum using a room temperature ionic liquid electrolyte. This coelectrodeposition enables the *in situ* integration of aluminum into the silicon deposit. The resulting Si-Al/TiO₂ nanotube nanocomposite anode exhibits improved cyclic stability and enhanced rate capability. The observed enhancement in battery electrochemical performance underscores the significance of this electrochemical process in fabricating such nanostructured silicon negative composite electrodes.

1. Introduction

Due to their high lithium storage capacities and low charge/discharge voltages, lithium alloying materials such as Si, Al, Sn, and Ge are of great interest as anode materials for Li-ion batteries.^[1–6] Among them, silicon particularly exhibits the highest theoretical specific capacity up to 3579 mAh g⁻¹ for Li₁₅Si₄,^[7–10] while aluminum

provides a theoretical specific capacity up to 993 mAh g⁻¹ for LiAl,^[11–13] which are 3–10 times higher than the current graphite anode. Their low charge/discharge potentials (0.3–0.4 vs Li⁺/Li) enable these materials to deliver high energy densities. However, their practical utilization is still limited by large volume expansion up to 300% for the Li₁₅Si₄ and 97% for that of LiAl during lithium insertion.^[3,14,15] This substantial change in volume generates internal stresses in particles, causing particle pulverization, breaking of solid electrolyte interface (SEI) layer and electrical losses of contacts within the electrode, leading to rapid capacity degradation.

Various attempts have been made to improve the cyclic stability of anodes through the use of nanostructures,^[16] composites,^[17] amorphous structures,^[18] and thin films.^[18] It has been suggested that silicon thin films and nanostructures could exhibit satisfactory cyclic performance due to their short electronic/ionic pathways and ability to relax strain.^[19–23] However, in the case of thin films, the active mass within nanometer scale is quite low to deliver sufficient capacity per unit area, and an increase of the thickness leads to large volume expansion, poor electric conductivity, especially for amorphous Si, eventual to capacity fading. In the case of nanostructures, the growth of silicon nanostructure such as nanotubes and nanowires is costly, complex, and involves several steps.^[24,25]

In order to increase the active mass and to develop effective nanostructure growth process, the interest of high surface area electroactive 3D substrate has been demonstrated in our previous work.^[26,27] We have shown an improvement in the cyclic stability of amorphous silicon (a-Si) film conformally electrodeposited on amorphous TiO₂ nanotubes in a form of Si/TiO₂ nanotube composite anode. By employing a similar procedure, we could electrodeposit aluminum onto TiO₂ nanotubes, forming an Al/TiO₂ nanotube nanocomposite structure.^[28] In these

A. W. Nemaga, J. Mallet

Laboratoire Lumière, nanomatériaux, nanotechnologies, L2n
Université de technologies de Troyes
CNRS UMR 7076
Université de Reims Champagne-Ardenne
Campus du moulin de la Housse, 51685 Reims Cedex2, France
E-mail: jeremy.mallet@univ-reims.fr

A. W. Nemaga, C. Guery, M. Morcrette
Laboratoire de Réactivité et Chimie des Solides, LRCS
CNRS UMR 7314
Université de Picardie Jules Verne
33 Rue Saint-Leu, Amiens 80039, Cedex, France
E-mail: mathieu.morcrette@u-picardie.fr

C. Guery, M. Morcrette
Réseau sur le Stockage Electrochimique de l'Energie (RS2E)
CNRS FR3459
33 Rue Saint Leu, Amiens 80039, Cedex, France

M. Molinari
Methodological Developments in Atomic Force Microscopy for Biology
Université de Bordeaux
CNRS, Bordeaux INP, CBMN, UMR 5248
F-33600 Pessac, France

J. Michel
Laboratoire Pathologies Pulmonaires et Plasticité Cellulaire
P3Cell, Unité INSERM UMR-S 1250
Université de Reims Champagne-Ardenne
21 rue Clément Ader, 51685 Reims, France

 Supporting information for this article is available on the WWW under https://doi.org/10.1002/batt.202500017

nanostructures, the TiO_2 nanotube support plays key roles through providing high surface area, direct contact with Ti current collector (thus avoiding addition of inactive binder), rough surface for good adhesion, and mechanically stable framework. Unlike most common template-assisted methods, the TiO_2 nanotube support does not need to be removed after coating due to its electroactivity, thereby avoiding mechanical damage during the template removing process. Although the previously studied Si/ TiO_2 composite exhibited improved cyclic stability, the rate capability of the composite still needs improvement especially at high Si loading due to the insulating nature of intrinsic amorphous Si deposit. To enhance the rate performance, the Si deposit could be mixed with conductive materials to improve the rate capability without deteriorating the cyclability. In this work, we unveiled the interest of incorporating Al in the Si deposit, as Al is both one of the best electrical conductors and electroactive versus lithium.^[29–32] Although the present study focuses on the battery application, aluminum-incorporated silicon nanostructure could also bring great interest for many technological applications due to the multifunctional property of the materials.

Among various nanostructure growth techniques such as vacuum techniques,^[33–35] the electrodeposition^[36] method is particularly interesting because it is relatively cheaper, no-constraining conditions and is handy to scale up. More importantly, it allows complete coating of complex geometry such as TiO_2 nanotubes which could not be achieved by other methods, for instance, by chemical vapor deposition,^[35] where only the upper part of the nanotubes was coated. Additionally, the structure, morphology, and composition of the deposits can be adjusted by easily controllable parameters such as voltage, current, and bath composition.^[37,38] Silicon and aluminum can only be electrodeposited from organic solvents, molten salts,^[39] or ionic liquids^[40] electrolytes due to their high negative reduction potentials and the high reactivity of their common precursors (e.g., SiCl_4 and AlCl_3) with water, which limits the use of aqueous solvents. Additionally, the use of organic solvents is also limited by low ionic conductivity, high volatility, and flammability. On the other hand, the molten salt electrolytes are also limited by the use of high-temperature process (500 °C–1000 °C). Nevertheless, Si and Al can effectively be electrodeposited from room-temperature ionic liquids (RTILs) thanks to their unique physicochemical and electrochemical properties such as low vapor pressure, high electrochemical

window (6 V), good ionic conductivity (no need of supporting electrolyte), good thermal stability, and nonflammability.^[41,42]

The present study demonstrates the electrochemical incorporation of Al into Si nanostructure by simple and cost-effective single-step coelectrodeposition method using RTILs. Si and Al (Si-Al) were codeposited on amorphous TiO_2 nanotubes and the resulting nanostructure (Si-Al/ TiO_2 nanotube composite) is characterized and tested as anode material for Li-ion batteries. To our knowledge, no studies deal with Al-incorporated Si nanostructure using electrodeposition method, so this study can provide important information on the material synthesis and applications.

2. Results and Discussion

2.1. TiO_2 Nanotubes Growth and Characterization

Fabricating TiO_2 nanotubes by the anodization method has been selected due to its ability to produce self-organized nanotubes that are well supported on the Ti substrate. The nanotubes, grown directly from the Ti substrate, serve as a template for electrodeposition in the subsequent step as demonstrated in our previous works. Figure 1a depicts the top view and cross-sectional (inset) scanning electron microscope (SEM) images of the as-anodized TiO_2 nanotubes formed after anodizing in diethylene glycol electrolyte with 2 wt% fluoric acid (HF) (50% v/v) and 2 wt% H_2O at 60 V for 17 h. It is evident that well-ordered TiO_2 nanotube arrays are directly grown from the Ti substrate. As previously described, the formation of these nanotubes results from simultaneous electrochemical oxidation and chemical dissolution reactions occurring during the anodization process.^[43–45] In this specific study, the interest lies in utilizing TiO_2 nanotubes as a high surface area, electroactive template for silicon and aluminum electrodeposition. Previous research on the deposition onto TiO_2 nanotubes indicates that the electrodeposition preferentially occurs on the external walls of the nanotubes.^[45–47] Therefore, the nanotubes are engineered with significant interspacing between nanotube walls to enhance the thickness of the deposit, thereby achieving high capacity per unit area. The obtained TiO_2 nanotubes exhibit an inner diameter ranging from 150 to 200 nm, a length of 3–4 μm and interspacing around 100–300 nm.

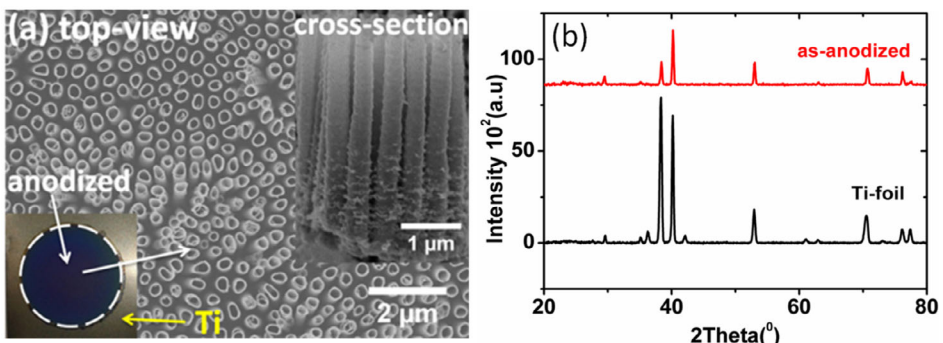


Figure 1. a) Top-view and cross-sectional (inset) SEM images of as-anodized TiO_2 nanotube arrays and b) the GIXRD patterns of the TiO_2 nanotubes in comparison with Ti foil patterns.

Figure 1b illustrates the grazing incidence X-ray diffraction (GIXRD) patterns of the as-anodized TiO_2 nanotubes compared with those of Ti foil. A GIXRD configuration with a 3° angle of incoming X-rays was employed to mitigate the dominance of peaks originating from the Ti substrate. The absence of typical crystalline TiO_2 peaks, aside from those arising from the Ti substrate, serves as evidence of the amorphous nature of the as-anodized nanotubes.^[48] Thermal treatment can induce a transformation from amorphous phase to the crystalline phase.^[48–50] However, studies indicate that the silicon deposited on amorphous phase demonstrates improved electrochemical performance compared to silicon deposited on anatase phase.^[27,51] Consequently, this study exclusively focuses on electrodeposition on the amorphous structure of the TiO_2 nanotubes.

2.2. Single-Step Si-Al Coelectrodeposition on Amorphous TiO_2 Nanotubes

The amorphous TiO_2 nanotube arrays served as a template for Si and Al electrodeposition from $[\text{P}_{1,4}]$ TFSA ionic liquid. Figure 2a shows the cyclic voltammetry (CV) of pure $[\text{P}_{1,4}]$ TFSA (dash line) and $[\text{P}_{1,4}]$ TFSA with 0.1 M SiCl_4 (solid line), while Figure 2b displays the CV of $[\text{P}_{1,4}]$ TFSA with 1.0 M AlCl_3 , and Figure 2c presents the CV of $[\text{P}_{1,4}]$ TFSA containing both 0.1 M SiCl_4 and 1.0 M AlCl_3 . All CVs were recorded at a scan rate of 10 mV s^{-1} at 50°C . With pure $[\text{P}_{1,4}]$ TFSA, no significant current is observed until reaching its cathodic limit, occurring at -3.2 V versus Pt (quasi-reference electrode [QRE]). This indicates the electrochemical stability of the

ionic liquid for the Si, Al, and Si-Al electrodeposition. The CVs measured with $[\text{P}_{1,4}]$ TFSA containing 0.1 M SiCl_4 , 1.0 M AlCl_3 , or both 0.1 M SiCl_4 and 1.0 M AlCl_3 exhibited broad cathodic reduction peaks starting at around -2.5 V versus Pt (QRE) associated with the reduction of Si^{4+} , Al^{3+} , or coreduction of $\text{Si}^{4+}/\text{Al}^{3+}$, respectively. No distinctly separated peaks are observed for Si-Al coreduction, possibly due to the overlapping range of the reduction potentials of the two elements. The minor current measured around -1.4 V may be due to the reduction of adsorbed species or electrolyte impurities.^[52]

Figure 2d displays typical current versus time ($I-t$) curves of Si, Al, and Si-Al electrodeposition on the TiO_2 nanotube template at -2.5 V versus Pt (QRE) at 50°C . The black line corresponds to pure Si growth from 0.1 M SiCl_4 , the red line corresponds to pure Al growth from 1.0 M AlCl_3 , and the blue line corresponds to Si-Al codeposition from 0.1 M SiCl_4 /1.0 M AlCl_3 electrolytes. In all cases, the rapid drop in currents within the first few seconds is attributed to ion depletion at the interface. Subsequently, the currents increase over the next few seconds as nucleation creates higher active surfaces favoring the electrodeposition.^[53] Finally, the current continuously decreases with time for Si due to its insulating nature, while it remains constant for Al, indicating its better electronic conductivity. In the case of Si-Al codeposition, the current drop is lower than that of Si, suggesting that the incorporated Al might provide better conductivity to the Si-Al deposit. Comparison of the bulk-deposition current (after 200 s) reveals that the current behavior of the Si-Al codeposition is quite similar to that of Si deposition, indicating that the codeposit is Si-rich.

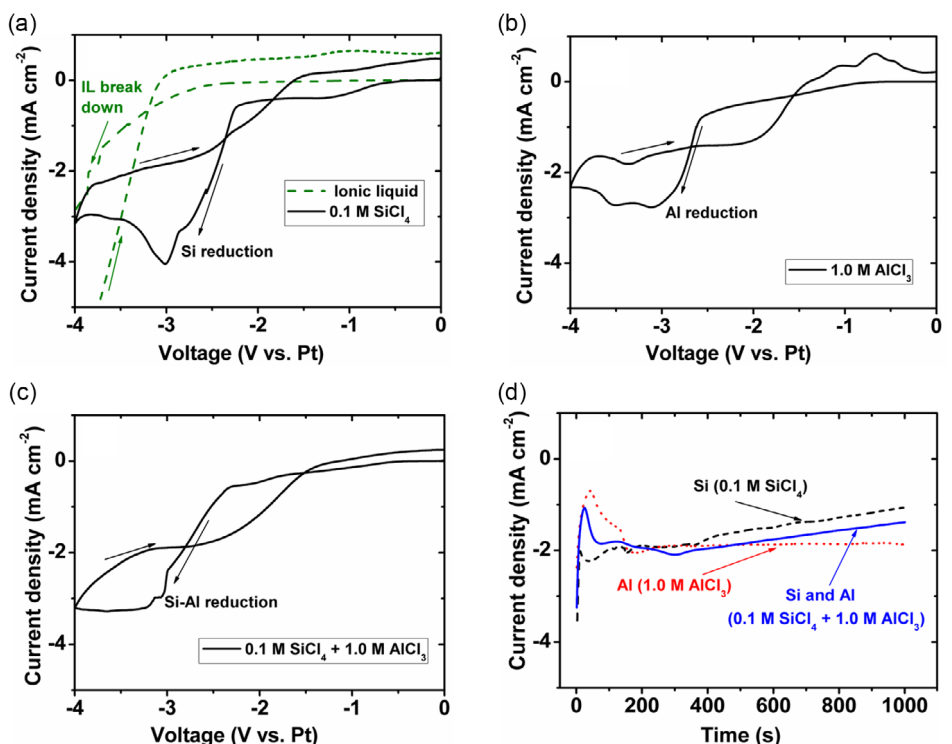


Figure 2. a) CV curves comparing pure $[\text{P}_{1,4}]$ TFSA (dash line) with $[\text{P}_{1,4}]$ TFSA containing 0.1 M SiCl_4 (solid line), b) $[\text{P}_{1,4}]$ TFSA with 1.0 M AlCl_3 , and c) $[\text{P}_{1,4}]$ TFSA with both 0.1 M SiCl_4 /1.0 M AlCl_3 , all at scan rate of 10 mV s^{-1} on a TiO_2 nanotube substrate. d) $I-t$ curves for pure Si (black line), pure Al (red line), and Si-Al (blue line) deposition on the TiO_2 nanotubes at -2.5 V versus Pt (QRE). The temperature deposition was fixed at 50°C .

Figure 3 presents SEM top-view and cross-sectional images of Si/TiO₂ nanotube (a) and amorph/TiO₂ nanotube (b) nanocomposites with a deposit loading of 1.8 C cm⁻² of electrochemical charge measured during the electrodeposition process. The morphologies of the images clearly depict the successful electrodeposition of Si or Si-Al on the TiO₂ nanotube surfaces, respectively. It is evident that the Si thin film uniformly coats the entire nanotube surfaces (Figure 3a, inset). Conversely, the Si-Al codeposit exhibits very similar growth as the silicon thin film, fully covering the nanotube surfaces from bottom to top (Figure 3b, inset). The successful complete coating of the TiO₂ nanotubes is a key aspect of the electrodeposition method, which is scarcely achieved by other techniques.^[35] Upon careful examination of the cross-sectional images of broken nanotubes (Figure S1, Supporting Information), it can be inferred that the deposition predominantly occurs on the outer surfaces of the TiO₂ nanotubes, filling the spaces between the nanotubes rather than completely filling the inside of the nanotube pores. This could be attributed to less effective ion diffusion into the nanotube pores compared to the wide cross-sectional space between nanotube walls.

To analyze the chemical composition of the Si-Al codeposit, energy-dispersive X-ray spectroscopy (EDX) analysis was performed simultaneously with imaging. Figure 3c displays the EDX spectra of the Si-Al/TiO₂ nanotubes collected from the top surface of the electrode, compared with the spectra of TiO₂ nanotubes and Si/TiO₂ nanotube composite. The spectrum obtained from the Si-Al/TiO₂ nanotube composite exhibits signals of Si and Al, confirming the codeposition of the two elements. The signal intensity of Al in the codeposit is lower than that of Si, with an Al:Si atomic percentage ratio of 20–25 at%, indicating that the deposit is Si-rich. The minor presence of Al in the codeposit compared to Si may be due to the electroactive species

originating from 1.0 M AlCl₃ being less abundant than those generated from 0.1 M SiCl₄ in the electrolyte. This dependence on concentration is because Al electrodeposition from the ionic liquid relies heavily on the concentration, and its reducible species (Al₂Cl₇⁻) exist only in saturated AlCl₃ solutions.^[54] Additionally, it may be related to the diffusion phenomena of the different forms of ionic species in the electrolyte, as the AlCl₃ generates different ionic complexes.^[42]

To gain further insights into the chemical composition and distribution of the codeposits, scanning transmission electron microscopy (STEM) investigations coupled with EDX analysis were conducted. **Figure 4a** presents a typical STEM dark-field image of the Si-Al-coated TiO₂ nanotube with a loading of 1.8 C cm⁻² of electrochemical charge measured during the electrodeposition process. The image illustrates a representative 2.5 μm long Si-Al/TiO₂ nanotube. A careful examination of the STEM dark-field image confirms the presence of a uniform thin film outside the TiO₂ nanotube, from bottom to top, indicating successful conformal coating along the entire nanotube surface via electrodeposition. The composition and homogeneity in the distribution of different elements along the nanotube were analyzed by performing EDX elemental mapping. The presence of Ti in the EDX image originates from the TiO₂ nanotube (Figure 4b). The more intense Ti contrast on one side of the nanotube is attributed to the top parts of the nanotubes being etched with HF for a longer duration during anodization compared to the bottom parts, resulting in thinner nanotubes at the top. Thus, the side of the nanotube with more intense Ti contrast is designated as the bottom part. The oxygen contrast becomes more intense, especially at the top, compared to Ti due to surface oxidation of the Si-Al deposit when the sample is exposed to ambient atmosphere (Figure 4c).

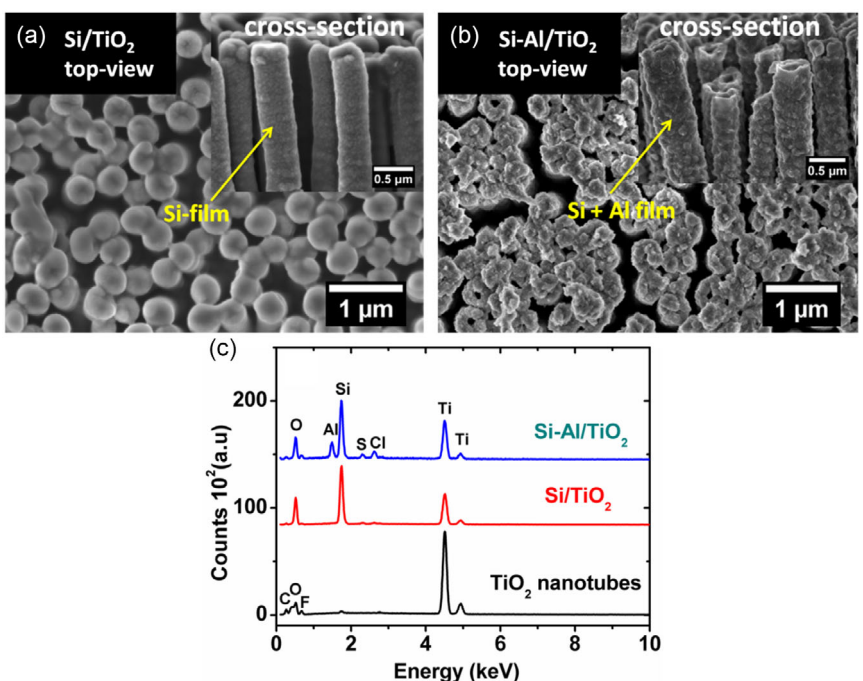


Figure 3. Top-view and cross-sectional SEM images of TiO₂ nanotubes after coated with Si a) and Si-Al b) with 1.8 C cm⁻² electrochemical charge. c) The corresponding EDX spectra collected through top-view image mapping.

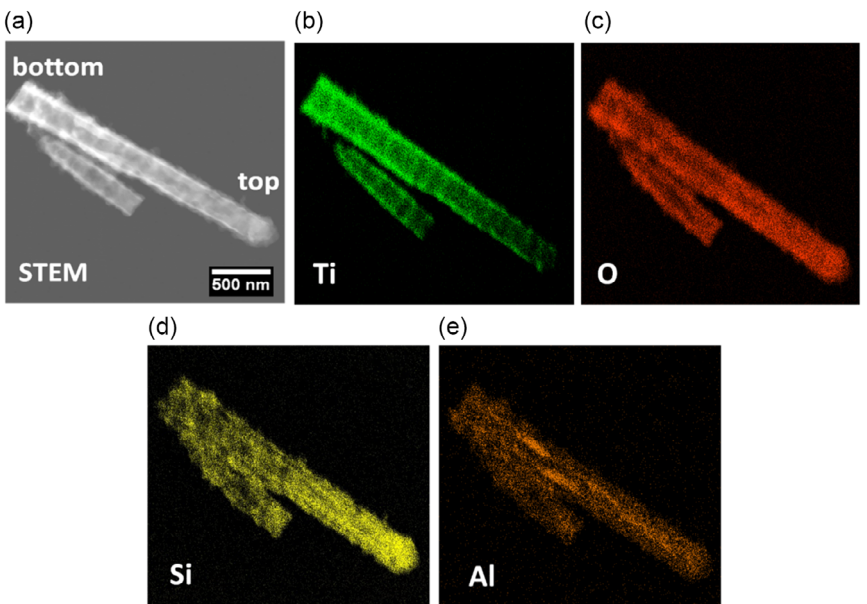


Figure 4. a) STEM dark field image of Si-Al/TiO₂ nanotube composite with 1.8 C cm⁻² electrodeposition charge and the corresponding EDX elemental mapping of b) Ti, c) O, d) Si, and e) Al.

Figures 4d,e depicts the elemental mappings of Si and Al in the codeposit, respectively. The denser contrast of Si mapping compared to Al mapping quantitatively implies the presence of more Si in the deposit than Al (with an Al:Si atomic% ratio of 20–25 at%), consistent with the SEM/EDX results (Figure 3c). The mapping reveals homogeneous distributions of Si and Al throughout the length of the nanotube, indicating that the coelectrodeposition technique facilitates *in situ* incorporation of Al in the Si deposit. It is noteworthy that according to the Al–Si binary phase diagram, Al has almost zero solid solubility in silicon (no beta phase), and silicon solubility in Al is quite low in the absence of a third element, thus the codeposit does not form a real Si–Al alloy.^[55,56] The Al is uniformly distributed along the TiO₂ nanotube, but in small areas, the Al contrast is more intense (Figure 4e), possibly due to the presence of local Al-rich grains. Since Al is distributed throughout the nanotubes, improved conductivity of the composite is expected. The single-step electrochemical approach is effective in this regard as it enables *in situ* incorporation of Al in the Si nanostructure. Such a nanocomposite is of considerable interest due to the various applications of Si and Al nanostructures, in addition to their use as negative electrodes for Li-ion batteries.

As revealed by the EDX investigations, the Si–Al codeposit obtained from the 0.1 M SiCl₄/1.0 M AlCl₃ electrolyte composition is Si-rich. For such composition, TEM characterization confirms that Si–Al deposit is amorphous. However, the quantity of Al incorporated in the codeposit can be increased by raising the concentration of AlCl₃ in the electrolyte (see Figure S2 and S3, Supporting Information). Codepositing Si–Al using 0.1 M SiCl₄/1.6 M AlCl₃ electrolyte compositions results in an Al-rich deposit (Figure S3, Supporting Information). Nevertheless, this study specifically focuses on the Si-rich deposit with a lower content of Al because it provides conformal coating, good adhesion, and higher capacity compared to Al rich composite, due to

higher theoretical capacity of Si compared to Al one. To achieve different structures, a two-step deposition process could be employed by first depositing Al on the TiO₂ nanotubes followed by Si deposition in the second step to obtain a Si/Al/TiO₂ layer-by-layer structure (refer to the *I-t* curves and the SEM/EDX profile in Figure S4 and Figure S5, Supporting Information respectively). Unfortunately, this composite exhibited poor cyclic stability as a negative electrode due to a nonconformal, crystalline Al intermediate layer (Figure S6, Supporting Information). Conversely, when Si is deposited first, Al deposition in the second step proves ineffective primarily due to the poor electronic conductivity of the thick amorphous silicon covering the TiO₂ nanotube surface.

2.3. Controlling the Loading of Si–Al Deposit on the TiO₂ Nanotube Matrix

To attempt to adjust the quantity of Si–Al codeposit loaded on the TiO₂ nanotube matrix, a coulometric mode was employed during electrodeposition. The electrodeposition was conducted using 0.1 M SiCl₄/1.0 M AlCl₃ electrolyte compositions until reaching a predefined electrochemical charge. As shown in Figure 3b, SEM images of the Si–Al/TiO₂ nanotube composite with a loading of 1.8 C cm⁻² of electrochemical charge measured during Si–Al coelectrodeposition reveal that at this charge limit, the TiO₂ nanotubes are completely covered with the deposit and are capped at the top. Despite this loading, there are still spaces between the nanotubes, allowing for further increase in the thickness of the deposit. Upon increasing the electrochemical charge limit to 2.8 C cm⁻², the nanotube matrix became completely filled with a thicker deposit (Figure 5). The denser deposit obtained with the higher electrochemical charge indicates that increasing the charge also increases the Si–Al loading on the TiO₂ nanotube template.

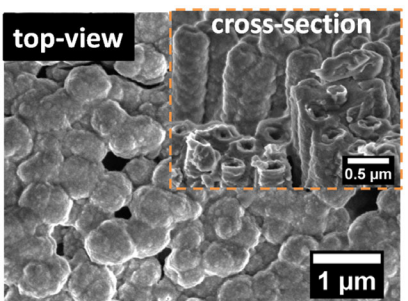


Figure 5. Top-view and cross-sectional (inset) SEM images of Si-Al/TiO₂ nanotube composite with 2.8 C cm⁻² electrochemical charge.

2.4. Electrochemical Performance of Si-Al/TiO₂ Nanotubes as Negative Electrode

The electrochemical performance of the Si-rich Si-Al/TiO₂ nanotube composites, obtained through a single-step coelectrodeposition of Si and Al, was studied as an anode material for Li-ion batteries. Figure 6a,b displays the first cycle galvanostatic discharge/charge profiles of the Si-Al/TiO₂ nanotube composites with two different loadings, in comparison with their respective Si/TiO₂ nanotube composites. All the discharge/charge curves exhibit two potential regions. The upper nondistinct potential region (3–1 V vs Li/Li⁺) corresponds to the typical monophasic lithiation/delithiation of amorphous TiO₂ nanotubes, while the lower potential region (1–0.01 V vs Li/Li⁺) is attributed to the alloying/dealloying of lithium with the deposits. In terms of discharge/charge voltage profile, there is no significant difference observed between the Si-Al/TiO₂ nanotube and Si/TiO₂ nanotube

electrodes (Figure 6a and b). However, the capacity contribution of the TiO₂ nanotubes to the composite electrodes is more pronounced in the Si-Al/TiO₂ composite than in the Si/TiO₂ composite. This could be due to the better conductivity of Al, which facilitates the lithiation of the inner core of the TiO₂ nanotubes in these composite structures. On the other hand, the capacity measured in the lower potential range with the Si/TiO₂ nanotube composite is higher than that measured with Si-Al/TiO₂ nanotube composite. This is primarily due to the higher theoretical capacity of Si compared to Al, given equivalent active mass of the deposits. Nevertheless, the total capacity obtained from the Si-Al/TiO₂ nanotube composite is higher compared to that of the Si/TiO₂ nanotube composite (Figure 6c,d).

To evaluate the capacities, the charge areal capacity was considered, as the discharge capacity is affected by SEI layer formation. The formation of SEI is also the primary reason for the irreversibility observed in the first cycle. The Si-Al/TiO₂ nanotube electrode with a 1.8 C cm⁻² electrochemical charge exhibited 1st and 80th cycle total areal charge capacities of 0.26 and 0.20 mAh cm⁻², respectively, with 99% coulombic efficiency at the 80th cycle (Figure 6c). When the electrochemical charge was increased to 2.8 C cm⁻², the 1st and 80th cycle total areal charge capacities also increased to 0.34 and 0.30 mAh cm⁻², respectively, with 99% coulombic efficiency at the 80th cycle (Figure 6d). The observed increase in capacity with electrochemical charge indicates that the electrochemical charge is reflective of the loading of the active mass. Compared to the Si/TiO₂ nanotubes, the Si-Al/TiO₂ nanotubes exhibited slightly higher capacity and better cyclability (Figure 6c,d). This suggests that the incorporated Al facilitates the lithiation/delithiation process during cycling. The observed

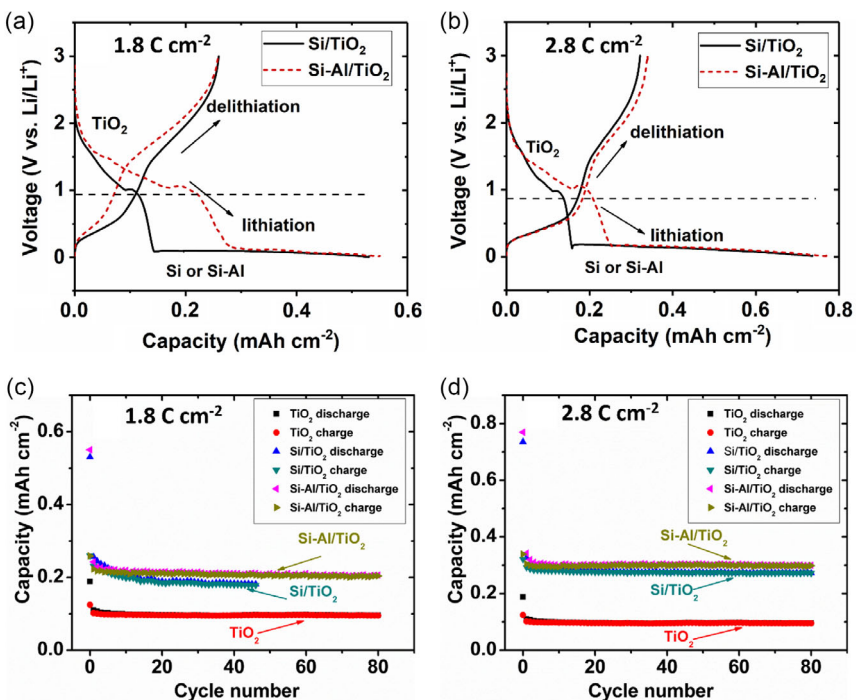


Figure 6. Half-cell coin-cell discharge/charge profiles of Si-Al/TiO₂ nanotubes with loadings of a) 1.8 C cm⁻² and b) 2.8 C cm⁻² electrochemical charges; c,d) the corresponding cyclic stability curves, respectively. The results are compared with the results of Si/TiO₂ nanotube electrodes.

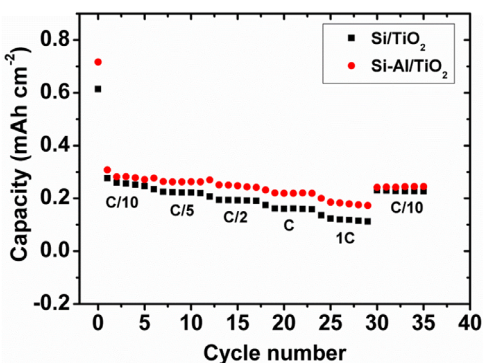


Figure 7. Half-cell coin-cell discharge capacity as a function of discharge rates for Si-Al/TiO₂ nanotube and Si-TiO₂ nanotube composite electrodes with 2.8 C cm⁻² electrochemical charge.

improved cycling performance of the composites provides evidence for the crucial role of nanostructured electrodes.

Since Al exhibits higher electronic conductivity than Si, the incorporation of Al is expected to improve the rate capability of the electrode. Therefore, rate capability studies on the Si-Al/TiO₂ nanotube composite at different rates were conducted. Figure 7 illustrates the discharge rate capability of the Si-Al/TiO₂ nanotube and Si/TiO₂ nanotube composites with a 2.8 C cm⁻² electrochemical charge. Since the three components of the composite electrodes have different C-rates, the applied C-rate for cycling is calculated based on silicon (Si), as it is the dominant component in terms of both quantity and capacity. Accordingly, the corresponding 1C current for a deposit of 2.8 C cm⁻² is estimated to be 730 μA cm⁻². The capacities of the two electrodes are equivalent at lower rates (C/10). However, the Si-Al/TiO₂ nanotube electrode exhibits a higher capacity than that of the Si/TiO₂ nanotube electrode at higher rates (\geq C/5). As the discharge rate increases, the capacity of Si/TiO₂ decreases faster than that of Si-Al/TiO₂, mainly because the intrinsic amorphous Si film is less electronically conductive. This illustrates that the Si-Al/TiO₂ nanotube composite provides better rate capability than the Si/TiO₂ nanotube composite.

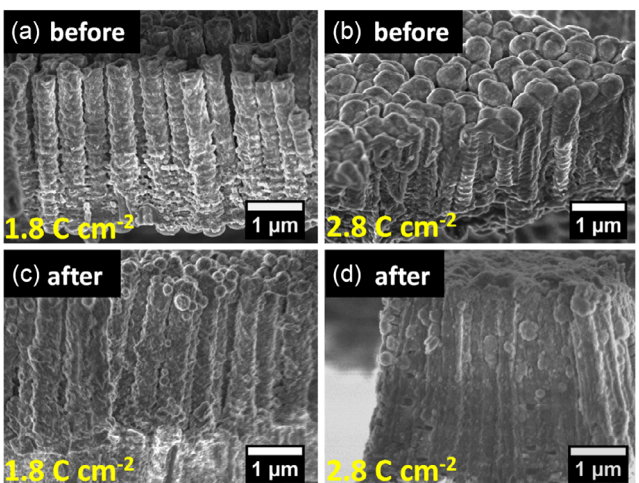


Figure 8. Cross-sectional SEM images of pristine Si-Al/TiO₂ nanotube composites with a) 1.8 C cm⁻² and b) 2.8 C cm⁻² electrochemical charges. The corresponding images after cycling are displayed on c) and d), respectively.

To confirm whether the nanostructures are preserved after cycling, SEM characterizations were performed. Figure 8 displays the cross-sectional SEM images of the pristine Si-Al/TiO₂ nanotube electrodes with 1.8 (a) and 2.8 C cm⁻² (b) electrochemical charges. The corresponding SEM images after 50 cycles are presented in Figure 8c,d, respectively. The interspaces between nanotubes decrease after cycling due to the volume increase upon lithiation. Especially with 2.8 C cm⁻², the nanotubes are merged through the deposit, indicating that the limit of the space between nanotubes has been reached. Interestingly, the nanostructures are maintained with no cracking or fracture of the deposit from the TiO₂ nanotube surface after 50 cycles, demonstrating the enhanced cycling performance of the Si-Al/TiO₂ nanotube composites.

3. Conclusion

The study reveals that Si and Al can be successfully codeposited using a single-step coelectrodeposition process in an ionic liquid containing both Si and Al precursors. STEM/EDX analysis confirms that Al is homogeneously distributed throughout the Si/TiO₂ nanotubes. The obtained nanostructure holds significant promise for numerous applications owing to the multifunctional properties of its components. The electrochemical performance of the Si-Al/TiO₂ nanotube composite, tested as a negative electrode for Li-ion batteries, demonstrated improved cyclic stability over 80 cycles. Although further studies including cycling beyond 200 cycles would provide more comprehensive insight into long-term performance and help rule out late-stage degradation mechanisms, the current results (obtained at an areal charge loading of 2.8 C cm⁻²) show a total areal capacity of 0.30 mAh cm⁻² with 88% capacity retention after 80 cycles. Compared to the Si/TiO₂ nanotube composite, the Si-Al/TiO₂ nanotube composite exhibited enhanced rate capability. The study suggests that the homogeneous distribution of Al within the Si nanostructure underscores the importance of the simple and cost-effective coelectrodeposition method for the growth of metal-incorporated silicon negative electrodes. In future work, this proof of concept will be extended by exploring alternative template materials with larger surface areas to increase active material loading and validate the scalability of the process. Additionally, the deposition of other high-capacity materials, such as Sn on hard carbon substrates, will be investigated to further enhance electrochemical performance for post-Li-ion battery technologies. These improvements are expected to pave the way for the development of next-generation nanostructured electrodes with optimized mechanical stability and electrochemical properties.

4. Experimental Section

TiO₂ Nanotubes Growth by Anodization

To fabricate highly ordered TiO₂ nanotubes, titanium foils (Goodfellow, 99.6%) with a thickness of 0.1 mm were subjected to anodization using a DC power supply (HP 6209B DC) coupled with a dual display multimeter (FLUKE 45), following the method

previously described.^[43] Initially, the titanium foils underwent sonication in acetone, isopropanol, and ethanol followed by rinsing in deionized water and drying in an argon stream. Subsequently the foils were anodized in a diethylene glycol electrolyte containing 2 wt% HF (50% v/v) and 2 wt% H₂O. The anodization process was conducted in two-electrode cell utilizing the titanium foil as working electrode (1.0 cm²) and platinum wire as counter electrode with the applied voltage of 60 V for 17 h. Then, the electrodes were immediately cleaned with acetone for 30 min and dried using an argon steam.

Single-Step Si-Al Coelectrodeposition on Amorphous TiO₂ Nanotubes from RTIL

Electrochemical studies were conducted using a Voltalab (PGZ 100) potentiostat controlled by voltamaster 4 software. All electrodeposition experiments were handled in an argon filled glove box with O₂ and H₂O content maintained below 2 ppm, as both the precursors and deposits are sensitive to air and moisture. The solvent used was 1-butyl-1-methylpyrrolidinium bis(trifluoromethanesulfonyl)imide ([P_{1,4}]TFSI) (Solvionic, 99.9%) RTIL. For Si and Al deposition, SiCl₄ (Sigma-Aldrich, 99.99%) and anhydrous powder of AlCl₃ (Sigma-Aldrich, 99.999%) were employed as precursors, respectively. Prior to Si-Al coelectrodeposition, the electrodeposition process of pure Si and pure Al on the TiO₂ nanotubes was investigated using 0.1 M SiCl₄ and 1.0 M AlCl₃ in the ([P_{1,4}]TFSI) ionic liquid, respectively. Higher concentration was utilized for Al precursor as it necessitated high concentration as previously reported.^[57,58]

Subsequently, a single-step Si-Al coelectrodeposition on the TiO₂ nanotubes was conducted using the same ionic liquid containing 0.1 M SiCl₄ and 1.0 M AlCl₃ to form Si-Al/TiO₂ nanotube nanocomposite. To ensure the purity of the ionic liquid, it was dried under vacuum at 100 °C for 72 h in the argon-filled glove box to reduce water content. The electrodeposition experiments were carried out potentiostatically at 50 °C in three-electrode cell using the TiO₂ nanotubes as working electrode, platinum wire as counter electrode, and platinum as QRE at -2.5 V versus Pt (QRE). The reference and counter electrodes were cleaned with acetone, ethanol, and deionized water through sonication, and then dried with hydrogen flam before cell construction. Postelectrodeposition, the electrodes were cleaned with dimethyl carbonate (DMC) to remove any residual electrolyte.

Materials Characterization

GIXRD with 3° angle of incoming X-rays was employed to examine the crystal structure of the as-anodized TiO₂ nanotubes. The structures, morphology, and compositions of the nanotubes before and after deposition were characterized using SEM (JEOL JSM 7900F) coupled with EDX. Furthermore, the structure and homogeneity of the incorporated Al in the codeposit were analyzed using STEM (JEOL 2100F) coupled with EDX mapping (JEOL JED 2300). The results of the Si-Al/TiO₂ nanotube composites were compared with those of the Si/TiO₂ nanotube composites.

Electrochemical Studies of the Si-Al/TiO₂ Nanotubes as Negative Electrode

The electrochemical performance of the Si-Al/TiO₂ nanotube composite was evaluated as anode in CR2032 half-cell coin cells. The coin cells were assembled in an argon-filled glove box with oxygen and water content maintained below 2 ppm. The setup utilized the Si-Al/TiO₂ nanotubes as working electrode, lithium foil as counter/reference electrode, and glass fiber separator soaked in 1 M LiPF₆ in ethylene carbonate/dimethyl (EC/DMC, 1:1 V/V) with 10% fluoroethylene carbonate (FEC) electrolyte solution (100 µL). Galvanostatic

discharge and charge cycles were conducted in a potential range of 0.01–3.0 V versus Li⁺/Li using VMP3 galvanostat/potentiostat workstation (BioLogic) controlled with EC-lab software.

Due to the varying mass and theoretical capacity of the composite components, the components have different C-rates. The electrodes were cycled at C/10 rate calculated for the Si, given its higher capacity contribution compared to other components. The Si-Al mass is determined based on the electrochemical charge measured during the electrodeposition process. However, related to the nature of the composite and the very small mass of the deposit in such microelectrodes, it is very difficult to determine accurately the mass of the deposits. To accurately determine the mass of the deposits, inductively coupled plasma (ICP) analysis was performed. However, this analysis yielded a large experimental error due to the composite's dissolution only in HF, which can also affect instrumental parts. Therefore, practical mass determination by ICP with HF solution proved complex. To minimize error from mass determination (due to the small amount of silicon and the potential entrapment of ionic liquid in the nanoporous matrix) and to enable consistent comparison with previous studies involving similar architectures, all capacities are reported as areal capacities (mAh cm⁻²).

Acknowledgements

The authors acknowledge the financial support provided by the Grand Est region, DRRT Grand Est, and FEDER funding for the Nano'Mat platform and PICT-URCA platform, which provided advance facilities to perform the SEM and STEM investigations. Additionally, the French Environment and Energy Management Agency (ADEME) is acknowledged for its financial support through a doctoral fellowship for a Ph.D. student. M.M. and C.G. thank the Labex STORE-EX project ANR-10-LABX-76-01 for its financial support. This work has been made within the framework of the Graduate School NANO-PHOT (École Universitaire de Recherche, contract ANR-18-EURE-0013).

Conflict of Interest

The authors declare no conflict of interest.

Data Availability Statement

The data that support the findings of this study are available from the corresponding author upon reasonable request.

Keywords: anode materials • electrodeposition • ionic liquids • lithium-ion batteries • Si-Al coelectrodeposition

- [1] P. U. Nzereogu, A. D. Omah, F. I. Ezema, E. I. Iwuoha, A. C. Nwanya, *Appl. Surf. Sci. Adv.* **2022**, *9*, 100233.
- [2] W.-J. Zhang, *J. Power Sources*, **2011**, *196*, 13.
- [3] M. Obrovac, V. Chevrier, *Chem. Rev.* **2014**, *114*, 11444.
- [4] D. Larcher, S. Beattie, M. Morcrette, K. Edstroem, J.-C. Jumas, J.-M. Tarascon, *J. Mater. Chem.* **2007**, *17*, 3759.
- [5] M. Thackeray, J. Vaughey, L. Fransson, *JOM* **2002**, *54*, 20.
- [6] W. Li, X. Sun, Y. Yu, *Small Methods* **2017**, *1*, 1600037.
- [7] M. Obrovac, L. Krause, *J. Electrochem. Soc.* **2007**, *154*, A103.
- [8] H. Tian, F. Xin, X. Wang, W. He, W. Han, *J. Materomics* **2015**, *1*, 153.
- [9] M. Ashuri, Q. He, L. L. Shaw, *Nanoscale* **2016**, *8*, 74.

- [10] K. Feng, M. Li, W. Liu, A. G. Kashkooli, X. Xiao, M. Cai, Z. Chen, *Small* **2018**, 14, 1702737.
- [11] Y. Hamon, T. Brousse, F. Jousse, P. Topart, P. Buvat, D. Schleich, *J. Power Sources* **2001**, 97, 185.
- [12] A. J. McAlister, *Bull. Alloy Phase Diagr.* **1982**, 3, 177.
- [13] S. K. Das, S. Mahapatra, H. Lahan, *J. Mater. Chem. A* **2017**, 5, 6347.
- [14] C. Zhang, F. Wang, J. Han, S. Bai, J. Tan, J. Liu, F. Li, *Small Struct.* **2021**, 2, 2100009.
- [15] M. Ko, S. Chae, J. Cho, *ChemElectroChem* **2015**, 2, 1645.
- [16] H. Li, X. Huang, L. Chen, G. Zhou, Z. Zhang, D. Yu, Y. J. Mo, N. Pei, *Solid State Ionics* **2000**, 135, 181.
- [17] M. Yoshio, H. Wang, K. Fukuda, T. Umeno, N. Dimov, Z. Ogumi, *J. Electrochem. Soc.* **2002**, 149, A1598.
- [18] S. Bourderau, T. Brousse, D. Schleich, *J. Power Sources* **1999**, 81, 233.
- [19] W. Qi, J. G. Shapter, Q. Wu, T. Yin, G. Gao, D. Cui, *J. Mater. Chem. A* **2017**, 5, 19521.
- [20] S. Ohara, J. Suzuki, K. Sekine, T. Takamura, *J. Power Sources* **2003**, 119, 591.
- [21] T. Moon, C. Kim, B. Park, *J. Power Sources* **2006**, 155, 391.
- [22] J. Maranchi, A. Hepp, P. Kumta, *Electrochem. Solid-State Lett.* **2003**, 6, A198.
- [23] N.-S. Choi, Y. Yao, Y. Cui, J. Cho, *J. Mater. Chem.* **2011**, 21, 9825.
- [24] T. Song, J. Xia, J.-H. Lee, D. H. Lee, M.-S. Kwon, J.-M. Choi, J. Wu, S. K. Doo, H. Chang, W. I. Park, *Nano Lett.* **2010**, 10, 1710.
- [25] B. Laik, L. Eude, J.-P. Pereira-Ramos, C. S. Cojocaru, D. Pribat, E. Rouvière, *Electrochim. Acta* **2008**, 53, 5528.
- [26] M. Zhao, J. Xiong, Y. Yang, J. Zhao, *ChemElectroChem* **2019**, 6, 3468.
- [27] A. W. Nemaga, J. Mallet, J. Michel, C. Guery, M. Molinari, M. Morcrette, *J. Power Sources* **2018**, 393, 43.
- [28] A. Woreka Nemaga, J. Mallet, C. Guery, M. Molinari, M. Morcrette, *J. Electrochem. Soc.* **2020**, 167, 112503.
- [29] S. S. Sharma, P. J. Crowley, A. Manthiram, *ACS Sustainable Chem. Eng.* **2021**, 9, 14515.
- [30] L. Chen, J. Xie, H. Yu, T. Wang, *Electrochim. Acta* **2008**, 53, 8149.
- [31] M. Fleischauer, M. Obrovac, J. Dahm, *J. Electrochem. Soc.* **2008**, 155, A851.
- [32] S.-O. Kim, A. Manthiram, *J. Mater. Chem. A* **2015**, 3, 2399.
- [33] M. Suzuki, J. Suzuki, K. Sekine, T. Takamura, *J. Power Sources* **2005**, 146, 452.
- [34] K.-S. Lee, Y.-L. Kim, S.-M. Lee, *J. Power Sources* **2005**, 146, 464.
- [35] J. Brumbarov, J. Kunze-Liebhäuser, *J. Power Sources*, **2014**, 258, 129.
- [36] W.-Q. Rong, J.-H. You, X.-M. Zheng, G.-P. Tu, S. Tao, P.-Y. Zhang, Y.-X. Wang, J.-T. Li, *ChemElectroChem* **2019**, 6, 5420.
- [37] W. Ruythooren, K. Attenborough, S. Beerten, P. Merken, J. Fransaer, E. Beyne, C. Van Hoof, J. De Boeck, J.-P. Celis, *J. Micromech. Microeng.* **2000**, 10, 101.
- [38] I. Dharmadasa, J. Haigh, *J. Electrochem. Soc.* **2006**, 153, G47.
- [39] G. M. Haarberg, O. Awayssa, R. Meirbekova, W. Xu, G. Saevardsdottir, *ECS Trans.* **2022**, 109, 155.
- [40] S. Thomas, D. Kowalski, M. Molinari, J. Mallet, *Electrochim. Acta* **2018**, 265, 166.
- [41] J. Robinson, R. Osteryoung, *J. Electrochem. Soc.* **1980**, 127, 122.
- [42] B. Welch, R. Osteryoung, *J. Electroanal. Chem. Interfacial Electrochem.* **1981**, 118, 455.
- [43] D. Kowalski, J. Mallet, J. Michel, M. Molinari, *J. Mater. Chem. A* **2015**, 3, 6655.
- [44] D. Kowalski, D. Kim, P. Schmuki, *Nano Today* **2013**, 8, 235.
- [45] D. Kowalski, J. Mallet, S. Thomas, A. W. Nemaga, J. Michel, C. Guery, M. Molinari, M. Morcrette, *J. Power Sources* **2017**, 361, 243.
- [46] D. Kowalski, A. Tighineanu, P. Schmuki, *J. Mater. Chem.* **2011**, 21, 17909.
- [47] D. Kowalski, P. Schmuki, *ChemPhysChem* **2012**, 13, 3790.
- [48] A. Tighineanu, T. Ruff, S. Albu, R. Hahn, P. Schmuki, *Chem. Phys. Lett.* **2010**, 494, 260.
- [49] R. Hahn, A. Ghicov, H. Tsuchiya, J. M. Macak, A. G. Muñoz, P. Schmuki, *Phys. Stat. Solidi* **2007**, 204, 1281.
- [50] G. F. Ortiz, I. Hanzu, P. Knauth, P. Lavela, J. L. Tirado, T. Djenizian, *Electrochim. Acta* **2009**, 54, 4262.
- [51] S. Ivanov, R. Grieseler, L. Cheng, P. Schaaf, A. Bund, *J. Electroanal. Chem.* **2014**, 731, 6.
- [52] J. M. Macak, B. G. Gong, M. Hueppe, P. Schmuki, *Adv. Mater.* **2007**, 19, 3027.
- [53] Y. ZHENG, S. ZHANG, L. Xingmei, W. Qian, Z. Yong, L. Lian, *Chin. J. Chem. Eng.* **2012**, 20, 130.
- [54] S. Z. El Abedin, E. Moustafa, R. Hempelmann, H. Natter, F. Endres, *Electrochem. Commun.* **2005**, 7, 1111.
- [55] J. Murray, A. McAlister, *Bull. Alloy Phase Diagr.* **1984**, 5, 74.
- [56] G. F. Vander Voort, J. Asensio-Lozano, *Microsc. Microanal.* **2009**, 15, 60.
- [57] S. Zein El Abedin, E. Moustafa, R. Hempelmann, H. Natter, F. Endres, *ChemPhysChem* **2006**, 7, 1535.
- [58] C. Lecoer, J.-M. Tarascon, C. Guery, *J. Electrochem. Soc.* **2010**, 157, A641.

Manuscript received: January 9, 2025

Revised manuscript received: April 25, 2025

Version of record online: April 29, 2025